Dirac boundary condition at the reconstructed zigzag edge of graphene

Ostaay, J.A.M. van; Akhmerov, A.R.; Beenakker, C.W.J.; Wimmer, M.

Dirac boundary condition at the reconstructed zigzag edge of graphene

J. A. M. van Ostaay, A. R. Akhmerov, C. W. J. Beenakker, and M. Wimmer
Instituut-Lorentz, Universiteit Leiden, P.O. Box 9506, NL-2300 RA Leiden, The Netherlands
(Received 5 September 2011; revised manuscript received 24 October 2011; published 8 November 2011)

Edge reconstruction modifies the electronic properties of finite graphene samples. We formulate a low-energy theory of the reconstructed zigzag edge by deriving the modified boundary condition to the Dirac equation. If the unit-cell size of the reconstructed edge is not a multiple of three with respect to the zigzag unit cell, valleys remain uncoupled and the edge reconstruction is accounted for by a single angular parameter ϑ. Dispersive edge states exist generically, unless $|\vartheta| = \pi/2$. We compute ϑ from a microscopic model for the "reczag" reconstruction (conversion of two hexagons into a pentagon-heptagon pair), and show that it can be measured via the local density of states. In a magnetic field, there appear three distinct edge modes in the lowest Landau level, two of which are counterpropagating.

DOI: 10.1103/PhysRevB.84.195434 PACS number(s): 73.22.Pr, 68.35.B−, 72.80.Vp, 73.21.Hb

I. INTRODUCTION

The bulk electronic properties of graphene[1] are modified by edge effects in a small sample. A prominent example is a narrow ribbon of graphene, which, depending on the exact lattice termination, is either gapped (semiconducting) or metallic.[2] Edge states may form a flat band, which favors spin polarization,[3,4] and may have applications in spintronics.[5] Scanning tunneling microscopy (STM) has provided considerable experimental support for these predicted edge effects.[6–9]

The honeycomb lattice of graphene can be terminated along different directions, with the zigzag and the armchair termination having the smallest unit cell [see Fig. 1(a)]. Recent microscopic calculations have indicated that these edges are unstable against a reconstruction of the hexagonal lattice structure, which increases the size of the unit cell.[10–16] In particular, Koskinen *et al.*[10] have shown that the lowest energy is reached for the zz(57) reconstruction of the zigzag edge: two adjacent hexagons convert into a pentagon-heptagon pair [see Fig. 1(b)]. The stability of this so-called "reczag" edge has been confirmed by a variety of theoretical calculations[11–16] and they have been observed by transmission electron microscopy.[17,18]

Electronic properties of the reczag edge (and related reconstructions) have been studied using the difference equations obtained from a tight-binding Hamiltonian on the terminated lattice.[19–21] In this paper, we propose an alternative approach based on the Dirac differential equation,[22,23] with edge reconstruction accounted for through a boundary condition.[24] The two approaches are equivalent at low energies, when the wavelength is large compared to the lattice constant. One advantage of the approach based on the Dirac equation is that it contains fewer independent parameters than the full tight-binding Hamiltonian. Another advantage is that the boundary conditions are strongly constrained by symmetry, providing a simple criterion for the existence of edge states and the presence or absence of intervalley scattering.

We show that a broad class of edge reconstructions can be described by a boundary condition governed by a single angular parameter ϑ. These boundaries cause no intervalley scattering and support dispersive edge states for $|\vartheta| \neq \pi/2$. The ϑ class of boundary conditions includes any edge reconstruction having a unit cell that is m times the size of a zigzag unit cell, with m not divisible by three. Most importantly, the reczag edge ($m = 2$) belongs to the ϑ class. The value of ϑ can be computed from a microscopic model (and we will carry out this calculation), but we also show how it can be directly measured by STM via the local density of states.

The paper is organized as follows. In Sec. II, we begin by discussing the general form of the boundary condition for reconstructed graphene edges and show how discrete symmetries can be used to reduce the number of free parameters to one single parameter (the ϑ-class boundary condition). We then focus in Sec. III on the particular case of the reczag boundary and compute the numerical value of ϑ from a tight-binding model. Sections IV and V are devoted to a calculation of the electronic structure of graphene terminated by reczag edges without and with magnetic field, respectively. We conclude in Sec. VI. The appendices contain details of the calculations as well as a discussion of the effects of next-nearest-neighbor hopping and edge potentials on the zigzag boundary condition (which also belongs to the ϑ class, having $m = 1$).

II. BOUNDARY CONDITION FOR RECONSTRUCTED EDGES

A. Tight-binding and Dirac Hamiltonian

We describe the electronic structure of graphene using the tight-binding Hamiltonian,

$$H = \sum_{i,j} t_{ij} |i\rangle\langle j| \tag{2.1}$$

with one orbital $|i\rangle$ per atom. In the bulk, we restrict ourselves to uniform nearest-neighbor hopping with value t. Only close to the edge we allow for a reconstruction of the honeycomb lattice and variations in the hopping amplitudes t_{ij}.

In the low-energy limit and sufficiently far from the boundary, excitations with energy ε obey the Dirac equation

$$H\Psi = \varepsilon\Psi, \tag{2.2}$$

where the Hamiltonian

$$H = v_{\mathrm{F}}\tau_0 \otimes (\boldsymbol{\sigma} \cdot \boldsymbol{p}) \tag{2.3}$$

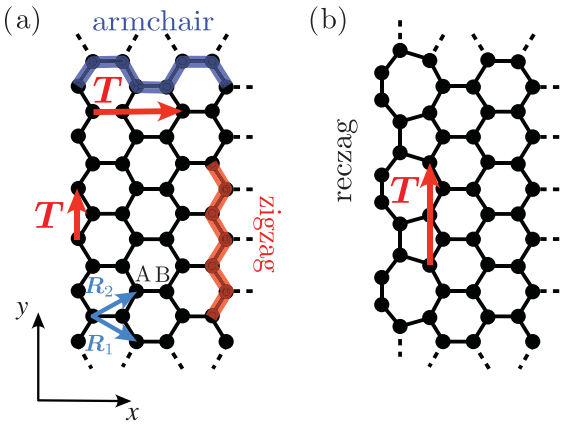

FIG. 1. (Color online) (a) Zigzag and armchair edge of the honeycomb lattice of graphene. (b) zz(57) or "reczag" reconstruction of the zigzag edge. The translation vector $\boldsymbol{T}$ of the various edges is indicated as well as the Bravais lattice vectors $\boldsymbol{R}_1$ and $\boldsymbol{R}_2$ of the honeycomb lattice (with two atoms A and B in the unit cell).

acts on a four-component spinor wave function,

$$\Psi = (\Psi_1,\Psi_2,\Psi_3,\Psi_4) = (\Psi_{\rm A}, -i\Psi_{\rm B}, i\Psi'_{\rm B}, -\Psi'_{\rm A}). \tag{2.4}$$

Here, $\Psi_{\rm X}$ and $\Psi'_{\rm X}$ denote the wave amplitude on the X $\in$ {A,B} sublattice in the valley K and K', respectively. The Fermi velocity is denoted by $v_{\rm F}$ and $\boldsymbol{p} = (-i\hbar\partial_x, -i\hbar\partial_y)$ is the two-dimensional momentum operator. The matrices τ_j and σ_j are the Pauli matrices in valley and sublattice space, respectively (with unit matrices τ_0 and σ_0).

The Dirac equation (2.2) has a sublattice (or "chiral") symmetry,

$$(\tau_z \otimes \sigma_z) H (\tau_z \otimes \sigma_z) = -H. \tag{2.5}$$

This symmetry implies that $H \mapsto -H$ for $\Psi_{\rm A} \mapsto \Psi_{\rm A}$ and $\Psi_{\rm B} \mapsto -\Psi_{\rm B}$. Physically, it expresses the fact that the nearest-neighbor hopping does not couple sites on the same sublattice. Chiral symmetry is preserved by lattice termination, but it is broken by edge reconstruction (which couples sites originating from the same sublattice).

B. Boundary conditions for broken chiral symmetry

The Dirac equation (2.2) must be supplemented by a boundary condition that also includes the effects of the edge reconstruction. In Ref. 24, it was shown that any valid current-conserving and time-reversal symmetric boundary condition for the Dirac equation has the form

$$\Psi = M\Psi, \quad M = (\boldsymbol{\nu}\cdot\boldsymbol{\tau})\otimes(\boldsymbol{n}\cdot\boldsymbol{\sigma}), \quad \boldsymbol{n}\perp\boldsymbol{n}_B\,, \tag{2.6}$$

where $\boldsymbol{n}_B$ is the unit vector in the $x-y$ plane normal to the boundary, and $\boldsymbol{\nu}$ and $\boldsymbol{n}$ are three-dimensional unit vectors. If the edge makes an angle α with the x axis, the boundary condition can be written more explicitly as

$$\Psi = (\boldsymbol{\nu}\cdot\boldsymbol{\tau})\otimes[\sigma_z\cos\vartheta + (\sigma_x\cos\alpha + \sigma_y\sin\alpha)\sin\vartheta]\Psi, \tag{2.7}$$

with $\theta \in (-\pi/2,\pi/2]$.

Chiral symmetry requires that $(\tau_z\otimes\sigma_z)M(\tau_z\otimes\sigma_z) = M$, which restricts the boundary condition (2.6) to zigzag ($\boldsymbol{\nu} = \pm\hat{z}$, $\boldsymbol{n} = \hat{z}$) or armchair ($\nu_z = n_z = 0$) form. Since edge reconstruction breaks chiral symmetry, other boundary conditions are allowed. Still, we can reduce the three independent parameters of the general boundary condition (2.6) to a single parameter for a broad class of edge reconstructions, as we will now show.

In the following, we consider edges that are invariant under a lattice translation $\boldsymbol{T} = n\boldsymbol{R}_1 + m\boldsymbol{R}_2$, $n,m\in\mathbb{Z}$, where $\boldsymbol{R}_1 = (\sqrt{3}a/2, -a/2)$ and $\boldsymbol{R}_2 = (\sqrt{3}a/2, a/2)$ are the two Bravais lattice vectors of graphene. Figure 1 shows the translation vector $\boldsymbol{T}$ for the example of the zigzag edge ($n=-1$, $m=1$), the armchair edge ($n=1$, $m=1$), and the reczag edge ($n=-2$, $m=2$). Due to the translational symmetry, the Bloch momentum $k \in [-\pi/|\boldsymbol{T}|, \pi/|\boldsymbol{T}|]$ along the boundary is a conserved quantum number. A zone-folding argument, detailed in Appendix A, shows that the two Dirac points of graphene project onto the same k if $n = m \bmod 3$ and different k otherwise. Conservation of k then implies that intervalley scattering is forbidden unless $n = m \bmod 3$.

These observations allow for some general statements: any reconstruction of the armchair edge has a translational vector $\boldsymbol{T}$ such that $n = m \bmod 3$, and hence allows for any three-parameter boundary condition (2.7). In contrast, any reconstruction of the zigzag edge has $n = -m$. Hence, if m is not divisible by three, the boundary condition does not mix valleys. In this case, $\nu = \pm\hat{z}$ and the boundary condition (for a given edge orientation α) has the single-parameter form

$$\Psi = \pm\tau_z\otimes[\sigma_z\cos\vartheta + (\sigma_x\cos\alpha + \sigma_y\sin\alpha)\sin\vartheta]\Psi, \quad \text{if } n \neq m \bmod 3. \tag{2.8}$$

The reczag boundary has a doubling of the unit cell with respect to zigzag ($m=2$) and hence has boundary condition of the form (2.8). If, however, the unit cell is a tripled (or a multiple of a tripled) zigzag unit cell, the general boundary condition (2.7) applies, i.e., valleys are typically mixed. An example of such an edge is the Z_{211} zigzag reconstruction discussed in Ref. 11.

In the remainder of the paper, we will focus on the reczag edge, since that has been predicted to be the most stable reconstruction.[10–16] However, we will give most of our results without specifying the angle ϑ, so that they apply to any edge with a boundary condition of the form (2.8). In order to emphasize this generality, we consider in Appendix B a zigzag edge where chiral symmetry is broken due to edge potentials or next-nearest-neighbor hopping, rather than due to edge reconstruction.

III. BOUNDARY CONDITION FOR THE RECZAG EDGE

A. Tight-binding model

In order to obtain a value for the angle ϑ in Eq. (2.8) for the reczag edge, we employ a tight-binding parametrization. We consider a reczag edge parallel to the y axis ($\alpha = 90^\circ$), as shown in Fig. 2. The unreconstructed edge would have terminated with an atom of the B sublattice, and we will therefore refer to the edge as the B-type reczag. (We give results for the A-type reczag at the end of the section.) The boundary condition for a B-type reczag edge along the y axis reads

$$\Psi = -\tau_z\otimes(\sigma_z\cos\vartheta + \sigma_y\sin\vartheta)\Psi. \tag{3.1}$$

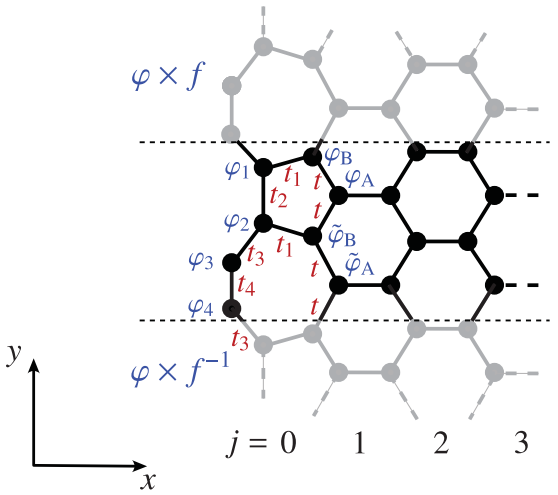

FIG. 2. (Color online) Nearest-neighbor tight-binding model of the reczag edge with identifiers for the hopping amplitudes (red) and the wave function amplitudes (blue). We take uniform hopping amplitudes t away from the edge. The unit cell of the reczag edge is indicated in dark, the neighboring unit cells are in light color. The wave functions in the neighboring unit cells are multiplied by a Bloch phase factor $f = e^{2ika}$.

We may write this boundary condition more explicitly in terms of the sublattice amplitudes (2.4),

$$\Psi_1 = i\mathcal{F}\Psi_2, \quad \Psi_3 = -i\mathcal{F}^{-1}\Psi_4, \tag{3.2}$$

$$\Psi_{\mathrm{A}} = \mathcal{F}\Psi_{\mathrm{B}}, \quad \Psi'_{\mathrm{A}} = \mathcal{F}\Psi'_{\mathrm{B}}, \tag{3.3}$$

with the definition

$$\mathcal{F} = \tan(\vartheta/2). \tag{3.4}$$

The reczag edge is translationally invariant over a distance $2a$, where a is the graphene lattice constant. Hence, wave functions in adjacent unit cells only differ by a phase $f = e^{2ika}$, with Bloch wave vector k. We allow for a variation of the hopping amplitude due to the reconstruction, but assume for simplicity that the hopping amplitude on every hexagon remains given by the bulk value t.

Numerical values for the modified hopping amplitudes from density functional theory (DFT) are in the literature[19] (see Table I). An extended model for the reczag edge with more parameters has been studied in Ref. 21. We give results for the extended model in Appendix C and show that there are no essential differences to the simpler model employed here. We also neglect the effects of hoppings beyond nearest-neighbor and edge potentials. These effects can all be accounted for by a modification of the numerical value of ϑ (see Appendices B and C).

TABLE I. DFT values for the hopping amplitudes t_p in the tight-binding model for the reczag edge, from Ref. 19, and the corresponding value of the boundary condition parameter $\mathcal{F} = \tan(\vartheta/2)$, calculated from Eq. (3.14).

t_1/t	t_2/t	t_3/t	t_4/t	$\mathcal{F}$	ϑ
0.91	0.99	0.97	1.5	0.0753	0.150

Labeling wave function and hopping amplitudes as indicated in Fig. 2, we can write down the tight-binding equations:

$$\varepsilon\varphi_B = t_1\varphi_1 + t\,(\varphi_A + f\tilde{\varphi}_A)\,, \tag{3.5a}$$

$$\varepsilon\tilde{\varphi}_B = t_1\varphi_2 + t\,(\varphi_A + \tilde{\varphi}_A)\,, \tag{3.5b}$$

$$\varepsilon\varphi_1 = t_1\varphi_B + t_2\varphi_2 + f t_3\varphi_4, \tag{3.5c}$$

$$\varepsilon\varphi_2 = t_2\varphi_1 + t_3\varphi_3 + t_1\tilde{\varphi}_B, \tag{3.5d}$$

$$\varepsilon\varphi_3 = t_3\varphi_2 + t_4\varphi_4, \tag{3.5e}$$

$$\varepsilon\varphi_4 = t_3\varphi_1/f + t_4\varphi_3. \tag{3.5f}$$

In the limit $\varepsilon \to 0$, it is now straightforward to find relations for the wave functions on the first hexagons away from the reconstructed edge,

$$\varphi_A = \frac{f t_1^2 t_4}{(1-f)t}\left(\frac{\varphi_B}{f t_3^2 - t_2 t_4} - \frac{\tilde{\varphi}_B}{t_3^2 - f t_2 t_4}\right), \tag{3.6a}$$

$$\tilde{\varphi}_A = \frac{t_1^2 t_4}{(1-f)t}\left(\frac{\tilde{\varphi}_B}{f^{-1} t_3^2 - t_2 t_4} - \frac{\varphi_B}{f t_3^2 - t_2 t_4}\right). \tag{3.6b}$$

B. Boundary modes

We proceed along the lines of Ref. 24, by separating the wave function ψ into a part Ψ that obeys the Dirac equation, plus a boundary correction $\psi_{\mathrm{bdy}}(\boldsymbol{r})$. Since the valleys are not coupled, it is sufficient to consider a single valley at $\boldsymbol{K} = (0, K) = (0, -4\pi/3a)$,

$$\psi_{\mathrm{A}}(\boldsymbol{r}) = \Psi_{\mathrm{A}}(\boldsymbol{r})e^{i\boldsymbol{K}\cdot\boldsymbol{r}} + \psi^{\mathrm{A}}_{\mathrm{bdy}}(\boldsymbol{r}), \tag{3.7a}$$

$$\psi_{\mathrm{B}}(\boldsymbol{r}) = \Psi_{\mathrm{B}}(\boldsymbol{r})e^{i\boldsymbol{K}\cdot\boldsymbol{r}} + \psi^{\mathrm{B}}_{\mathrm{bdy}}(\boldsymbol{r}). \tag{3.7b}$$

Taking further into account the translational symmetry along the y direction, we can write the wave function as

$$\psi_{\mathrm{A}}(\boldsymbol{r}) = \phi_{\mathrm{A}}(j)e^{iKy} + \phi^{\mathrm{A}}_{\mathrm{bdy}}(j)e^{i\tilde{K}y}, \tag{3.8a}$$

$$\psi_{\mathrm{B}}(\boldsymbol{r}) = \phi_{\mathrm{B}}(j)e^{iKy} + \phi^{\mathrm{B}}_{\mathrm{bdy}}(j)e^{i\tilde{K}y}, \tag{3.8b}$$

$$\tilde{K} = K + \pi/a = -\pi/3a. \tag{3.8c}$$

The index j numbers the unit cells transverse to the edge, with φ_B, $\tilde{\varphi}_B$ corresponding to $j = 0$ and φ_{A}, $\tilde{\varphi}_{\mathrm{A}}$ to $j = 1$ (see Fig. 2). We denote by $\tilde{K}$ the projection of the K point into the doubled unit cell of the reczag edge. The Dirac modes thus have a periodicity given by the unperturbed graphene lattice, whereas the boundary modes are governed by the periodicity of the reczag reconstruction. Application of the boundary condition (3.1) on the Dirac modes specifies the angle $\vartheta \in (-\pi/2, \pi/2)$ from

$$\phi_{\mathrm{A}}(0)/\phi_{\mathrm{B}}(0) = \tan(\vartheta/2). \tag{3.9}$$

For the bulk of graphene away from the edge, the tight-binding equations take the form

$$\varepsilon\psi_{\mathrm{A}}(\boldsymbol{r}) = t\,[\psi_{\mathrm{B}}(\boldsymbol{r}) + \psi_{\mathrm{B}}(\boldsymbol{r} - \boldsymbol{R}_1) + \psi_{\mathrm{B}}(\boldsymbol{r} - \boldsymbol{R}_2)]\,, \tag{3.10a}$$

$$\varepsilon\psi_{\mathrm{B}}(\boldsymbol{r}) = t\,[\psi_{\mathrm{A}}(\boldsymbol{r}) + \psi_{\mathrm{A}}(\boldsymbol{r} + \boldsymbol{R}_1) + \psi_{\mathrm{A}}(\boldsymbol{r} + \boldsymbol{R}_2)]\,. \tag{3.10b}$$

Inserting the decomposition (3.8) into Eq. (3.10) and accounting for the fact that the Dirac and boundary modes

have a different periodicity, we arrive in the limit $\varepsilon \to 0$ at

$$\phi_{\rm A}(j+1) = \phi_{\rm A}(j), \quad \phi^{\rm A}_{\rm bdy}(j+1) = \frac{1}{\sqrt{3}}\phi^{\rm A}_{\rm bdy}(j), \quad (3.11a)$$

$$\phi_{\rm B}(j+1) = \phi_{\rm B}(j), \quad \phi^{\rm B}_{\rm bdy}(j+1) = \sqrt{3}\phi^{\rm B}_{\rm bdy}(j). \quad (3.11b)$$

In order for the wave function to be normalizable, only nongrowing contributions are allowed, so $\phi^{\rm B}_{\rm bdy}(j) = 0$ for all j. The B-type reczag edge thus has a boundary mode on the A sublattice only. This boundary mode is a direct consequence of the unit cell doubling of the reconstructed edge.

The boundary mode decays exponentially away from the edge, with a decay length of $3a/2$. This is also the distance from the edge where the Dirac equation—which does not capture the boundary modes—is valid. Hence, the reczag edge can be faithfully treated within the Dirac approach, as there are deviations only within the first few unit cells away from the boundary.

C. Boundary condition

The wave amplitudes $\varphi_{\rm A,B}$ and $\tilde{\varphi}_{\rm A,B}$ near the reczag edge can be written in terms of the Dirac and boundary modes as

$$\varphi_{\rm A} = \left[\phi_{\rm A}(1) + \phi^{\rm A}_{\rm bdy}(1)\right] f^{-1/4}, \quad (3.12a)$$

$$\tilde{\varphi}_{\rm A} = \left[\phi_{\rm A}(1) - \phi^{\rm A}_{\rm bdy}(1)\right] f^{-3/4}, \quad (3.12b)$$

$$\varphi_{\rm B} = \phi_{\rm B}(0), \quad (3.12c)$$

$$\tilde{\varphi}_{\rm B} = \phi_{\rm B}(0) f^{-1/2}. \quad (3.12d)$$

With this decomposition, we find from Eq. (3.6) that

$$\phi_{\rm A}(0) = \mathcal{F}\phi_{\rm B}(0), \quad (3.13)$$

$$\mathcal{F} = \tan(\vartheta/2) = \frac{t_1^2 t_4\left(t_2 t_4 - t_3^2\right)}{2t\left(t_3^4 + t_2 t_3^2 t_4 + t_2^2 t_4^2\right)}. \quad (3.14)$$

The numerical values for $\mathcal{F}$ and ϑ for the reczag edge are given in Table I.

This concludes the derivation of the boundary condition for the B-type reczag edge. For the A-type reczag, the role of the A and B sublattices is interchanged. We thus have the boundary conditions

$$\Psi_1 = i\mathcal{F}^{-1}\Psi_2, \quad \Psi_3 = -i\mathcal{F}\Psi_4, \quad (3.15)$$

$$\Psi_{\rm B} = \mathcal{F}\Psi_{\rm A}, \quad \Psi'_{\rm B} = \mathcal{F}\Psi'_{\rm A}, \quad (3.16)$$

with the same value (3.14) of $\mathcal{F}$.

The zigzag boundary condition[2] corresponds to $\mathcal{F} = 0$ or $\mathcal{F} = \infty$. As one can see from Eq. (3.14), $\mathcal{F}$ vanishes if $t_3 = \sqrt{t_2 t_4}$, so for these matched hopping amplitudes the doubling of the unit cell at the edge has no effect on the boundary condition. This explains why a zigzag-edge behavior was found in a tight-binding study of edge reconstruction for the special case that all hopping amplitudes have their bulk values.[21]

IV. ELECTRONIC STATES

A. Dirac solutions

The knowledge of the boundary condition allows us to calculate electronic properties. In this section, we consider zero magnetic field and then in the next section, the effect of a magnetic field is included. Although we use the numerical values of the reczag edge obtained in the previous section for plots and comparisons to tight-binding models, the analytical results we obtain are valid for arbitrary angles ϑ.

Since the reczag edge does not mix the valleys, it is possible to consider the K and K' points separately. From Eqs. (3.2) and (3.15), we see that, given a solution for a particular valley, substitution of $\mathcal{F} \to -1/\mathcal{F}$ gives a solution in the other valley. In what follows, we focus our discussion on the K point.

We consider either one or two reczag edges along the y direction. The solution of the Dirac equation (2.3) at energy ε has the form $\Psi(x,y) = \psi(x)e^{iky}$ with

$$\psi(x) = A\begin{pmatrix} \frac{\hbar v_{\rm F}}{\varepsilon}(k+iq) \\ i \end{pmatrix} e^{iqx} + B\begin{pmatrix} \frac{\hbar v_{\rm F}}{\varepsilon}(k-iq) \\ i \end{pmatrix} e^{-iqx}. \quad (4.1)$$

The wave vector k is real, q is real or imaginary, and the dispersion relation is $\varepsilon = \pm\hbar v_{\rm F}\sqrt{k^2+q^2}$. The relative amplitudes A and B of the superposition have to be determined by the boundary condition.

B. Edge-state dispersion

To study the dispersion relation of the edge state, we take a semiinfinite graphene sheet for $x \geqslant 0$, terminated with a B-type reczag edge at $x = 0$. We first focus on decaying solutions with an imaginary $q = iz$ and energy $|\varepsilon| < |\hbar v_{\rm F} k|$. These edge states are affected most prominently by the edge reconstruction. Keeping only the exponentially decaying part of (4.1) and substituting the boundary condition (3.2), we find the equation

$$\hbar v_{\rm F}(z-k) = \mathcal{F}\varepsilon. \quad (4.2)$$

This only has a normalizable solution for

$$z = k\frac{1-\mathcal{F}^2}{1+\mathcal{F}^2} = k\cos\vartheta > 0. \quad (4.3)$$

The normalized edge state wave function then reads

$$\psi^{\rm edge}(x) = \begin{pmatrix} i\sin^2\vartheta/2 \\ \cos^2\vartheta/2 \end{pmatrix}\sqrt{2k\cos\vartheta}\, e^{-kx\cos\vartheta} \quad (4.4)$$

with energy[24,25]

$$\varepsilon(k) = -\hbar v_{\rm F} k\sin\vartheta, \quad \text{for } k\cos\vartheta > 0. \quad (4.5)$$

The solution for the K' valley is found by the replacement of $\mathcal{F} \to -1/\mathcal{F}$ in Eq. (4.2), yielding a solution with energy

$$\varepsilon(k) = \hbar v_{\rm F} k\sin\vartheta, \quad \text{for } k\cos\vartheta < 0. \quad (4.6)$$

These edge states exist for any $|\vartheta| < \pi/2$.

It is instructive to compare the reczag edge state with the well-known zigzag counterpart,[2,3] which corresponds to the limit $\vartheta \to 0$. In accord with the tight-binding calculations,[21] the main difference between the two types of edge states is their energy dispersion; while the zigzag edge state features a dispersionless band $\varepsilon(k) = 0$, the reczag edge state has a linear dispersion with velocity $v_{\rm F}\sin\vartheta$. This has implications for the density of states (see Sec. IV C).

Furthermore, the zigzag edge state is exactly zero on one sublattice (the A sublattice for a B-type zigzag edge), whereas the reczag edge couples the two sublattices. The coupling is

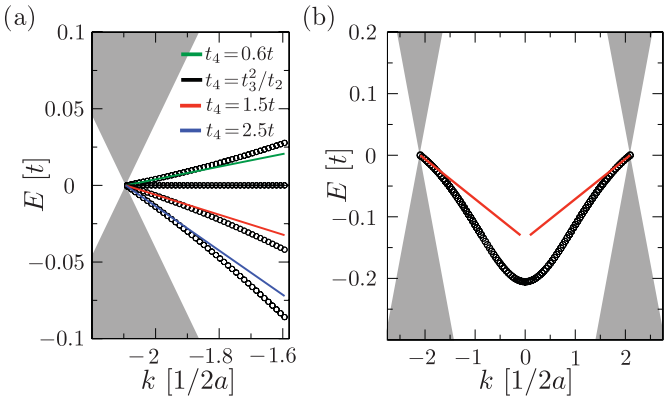

FIG. 3. (Color online) (a) Comparison between tight-binding (black circle) and Dirac equation results (solid lines) for the edge state dispersion near the K point. Results are shown for different values of the hopping amplitude t_4 of the reczag edge. (All other hopping amplitudes are as in Table I.) The continuum of bulk states in the Dirac cone is indicated in grey. (b) The data for $t_4 = 1.5t$ on a larger scale, showing both the K and K' points.

such that the two components of the wave function only differ by a constant factor, $\psi_1(x) = \mathcal{F}\psi_2(x)$ for all x, not only at the boundary. The wave function thus has the same decay length $(k\cos\vartheta)^{-1}$ into the bulk on each sublattice.[26] For $\vartheta \to \pi/2$, the decay length diverges and the edge state disappears in the bulk.

In Fig. 3(a), we compare the edge state dispersion (4.5) with the results of the tight-binding model of the reczag edge. (The tight-binding results were calculated for a nanoribbon of width $W = 1000\sqrt{3}a$, large enough that the opposite edges were essentially decoupled.) Results are shown for different values of $\mathcal{F}$, obtained by modifying the value of t_4 with respect to the DFT values in Table I. As expected, we find excellent agreement for small ε, corresponding to k values close to the K or K' points. Away from these Dirac points, the two disconnected edge states of the Dirac equation are connected by the tight-binding model, see Fig. 3(b).

C. Density of states

To make contact with STM experiments, we calculate the local density of states (DOS) on sublattice $j = \mathrm{A,B}$, given by

$$\mathcal{D}_j(\varepsilon,\boldsymbol{r}) = \sum_n \delta(\varepsilon-\varepsilon_n)[|(\Psi_n)_j(\boldsymbol{r})|^2 + |(\Psi'_n)_j(\boldsymbol{r})|^2]. \quad (4.7)$$

The sum runs over all eigenstates Ψ_n, Ψ'_n in valley K, K' with energy ε_n. For the reczag edge state, we find

$$\mathcal{D}_{\mathrm{A}}^{\mathrm{edge}}(\varepsilon,x) = \mathcal{F}^2\,\mathcal{D}_{\mathrm{B}}^{\mathrm{edge}}(\varepsilon,x), \quad (4.8a)$$

$$\mathcal{D}_{\mathrm{B}}^{\mathrm{edge}}(\varepsilon,x) = \frac{g_{\mathrm{s}}g_{\mathrm{v}}\cos^2(\vartheta/2)}{\pi\hbar v_{\mathrm{F}}\,|\sin\vartheta|}u\Theta(u)e^{-2ux},$$
$$\text{with}\ \ u = -\varepsilon(\hbar v_{\mathrm{F}}\tan\vartheta)^{-1}. \quad (4.8b)$$

The function $\Theta(u)$ is the unit step function [$\Theta(u) = 1$ for $u \geqslant 0$ and zero otherwise]. The coefficients $g_{\mathrm{s}} = g_{\mathrm{v}} = 2$ indicate the degeneracies due to the spin and valley degrees of freedom.

Integrating out the transverse coordinate x and summing over both sublattices, we find the total DOS per unit length of the edge,

$$\mathcal{D}^{\mathrm{edge}}(\varepsilon) = \frac{g_{\mathrm{s}}g_{\mathrm{v}}}{2\pi\hbar v_{\mathrm{F}}\,|\sin\vartheta|}\,\Theta(u). \quad (4.9)$$

This result holds in the energy range $|\varepsilon| \lesssim (\hbar v_{\mathrm{F}}/a)|\sin\vartheta|$ (beyond which the Dirac equation breaks down). Such a constant DOS was also found for the case when the edge state acquires a dispersion due to next-nearest neighbor hopping.[27,28] Compared to the zigzag case, where $\mathcal{D}^{\mathrm{edge}}(\varepsilon) \sim \delta(\varepsilon)$, the density of states is greatly reduced by the reconstruction, which may well prevent the ferromagnetic instability of the zigzag edge.[3]

In addition to the decaying edge state with imaginary q, there is a continuum of bulk states with real q. Then the term

$$\frac{\hbar v_{\mathrm{F}}}{\varepsilon}(k+iq) = \mathrm{sgn}(\varepsilon)\frac{k+iq}{\sqrt{k^2+q^2}} = \mathrm{sgn}(\varepsilon)\,e^{i\varphi} \quad (4.10)$$

in Eq. (4.1) is a pure phase (sgn is the sign function). These bulk solutions are given by

$$\psi^{\mathrm{bulk}}(x) = C_{\mathrm{bulk}}\begin{pmatrix} \sin qx + \mathrm{sgn}(\varepsilon)\,\mathcal{F}\sin(qx+\varphi) \\ i\,\mathrm{sgn}(\varepsilon)\sin(qx-\varphi) + i\mathcal{F}\sin qx \end{pmatrix}, \quad (4.11)$$

with $\hbar v_{\mathrm{F}} q = |\varepsilon|\sin\varphi > 0$ and normalization constant

$$C_{\mathrm{bulk}} = \pi^{-1/2}(1+\mathcal{F}^2+2\,\mathrm{sgn}(\varepsilon)\,\mathcal{F}\cos\varphi)^{-1/2}. \quad (4.12)$$

The local DOS of the bulk states follows upon integration,

$$\mathcal{D}_j^{\mathrm{bulk}}(\varepsilon,x) = \frac{g_{\mathrm{s}}g_{\mathrm{v}}|\varepsilon|}{2\pi\hbar^2 v_{\mathrm{F}}^2}\int_0^\pi d\varphi\,\left|\psi_j^{\mathrm{bulk}}(x)\right|^2. \quad (4.13)$$

For $\mathcal{F} \ll 1$, the integral can be evaluated analytically,

$$\mathcal{D}_{\mathrm{A}}^{\mathrm{bulk}}(x,\varepsilon) = \frac{g_{\mathrm{s}}g_{\mathrm{v}}|\varepsilon|}{4\pi\hbar^2 v_F^2}[1 - J_0(\xi) + 2\,\mathrm{sgn}(\varepsilon)\mathcal{F}J_1(\xi) + \mathcal{F}^2[J_0(\xi) - J_2(\xi)] + \mathcal{O}(\mathcal{F}^3)], \quad (4.14a)$$

$$\mathcal{D}_{\mathrm{B}}^{\mathrm{bulk}}(x,\varepsilon) = \frac{g_{\mathrm{s}}g_{\mathrm{v}}|\varepsilon|}{4\pi\hbar^2 v_F^2}\left[1 - J_2(\xi) + \mathrm{sgn}(\varepsilon)\mathcal{F}[J_3(\xi) - J_1(\xi)] + \frac{1}{2}\mathcal{F}^2[J_2(\xi) - J_4(\xi)] + \mathcal{O}(\mathcal{F}^3)\right], \quad (4.14b)$$

with $\xi = 2x|\varepsilon|/\hbar v_{\mathrm{F}}$. Away from the edge, $\mathcal{D}_{\mathrm{A}}^{\mathrm{bulk}} + \mathcal{D}_{\mathrm{B}}^{\mathrm{bulk}} \to g_{\mathrm{s}}g_{\mathrm{v}}|\varepsilon|/2\pi\hbar^2 v_F^2$ approaches the $\pm\varepsilon$-symmetric DOS of an infinite graphene sheet. The boundary effects break this electron-hole symmetry, as a manifestation of the chiral symmetry breaking by the reczag boundary condition.

Figure 4 shows the full local DOS on each sublattice, $\mathcal{D}_{\mathrm{X}} = \mathcal{D}_{\mathrm{X}}^{\mathrm{edge}} + \mathcal{D}_{\mathrm{X}}^{\mathrm{bulk}}$ with $\mathrm{X} \in \{\mathrm{A,B}\}$. The edge state manifests itself as a peak in the local DOS on the B sublattice. The DOS on the A sublattice is much smaller near the edge (by a factor $\mathcal{F}^2 \approx 0.006$). The peak energy $\varepsilon_{\mathrm{peak}}$ moves toward the Dirac point (the zero of energy) as the distance x from the edge is increased, according to

$$\frac{\varepsilon_{\mathrm{peak}}}{\hbar v_F} = \frac{\vartheta}{2x}, \quad (4.15)$$

for $x \gtrsim 3a/2$, $|\vartheta| \ll \pi/2$. (The Dirac approximation breaks down at smaller x, while for larger ϑ the edge DOS no longer dominates over the bulk DOS.) We conclude that STM

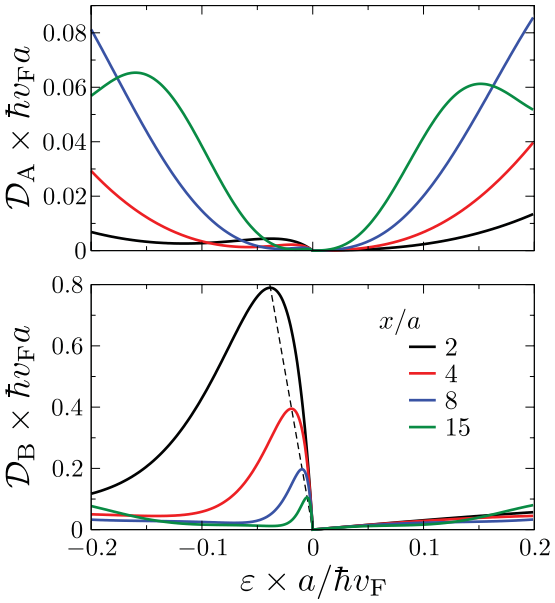

FIG. 4. (Color online) Local density of states as a function of energy at various distances from the reczag edge. The contributions from the A and B sublattices are shown separately in the two panels. The peak in the density of states evolves according to Eq. (4.15) (dashed line in lower panel).

experiments have direct access to the boundary condition angle ϑ, through the dependence of the edge-state peak on the distance from the edge.

D. Nanoribbon

So far, we considered a semiinfinite graphene sheet with a single B-type reczag edge. Reczag nanoribbons (width W) will have a B-type reczag edge on one side (at $x = 0$) and an A-type reczag edge at the other side (at $y = W$). The spectrum now consists of a discrete set of transverse modes $\varepsilon_n(k)$, governed by the transcendental equation[24]

$$\cos^2\vartheta\left(\cos\omega - \cos^2\Omega\right) - \sin^2\vartheta\cos\omega\cos^2\Omega + \sin\Omega\left(\sin\Omega - \sin\omega\sin 2\vartheta\right) = 0. \tag{4.16}$$

We defined $\omega^2 = 4W^2[(\varepsilon/\hbar v_F)^2 - k^2]$ and $\cos\Omega = \hbar v_F k/\varepsilon$.

Figure 5 compares the mode dispersion of a zigzag[2] ($\vartheta = 0$) and a reczag nanoribbon. The prominent difference is the dispersion of the reczag edge mode. For $kW\cos\vartheta \gg 1$, it is given (up to exponentially small corrections) by the results for a single edge, $\varepsilon(k) = \pm\hbar v_F|k|\sin\vartheta$, since then the wave functions on opposite edges decay rapidly and overlap only little. Both in the zigzag and reczag nanoribbons, the overlap of the edge states as $k \to 0$ produces a larger and larger energy splitting until the edge states merge with the bulk bands.

The bulk bands of the reczag nanoribbon have a slight offset toward negative energies (barely visible in Fig. 5), which breaks the electron-hole symmetry—again as a result of the breaking of chiral symmetry by the edge reconstruction.

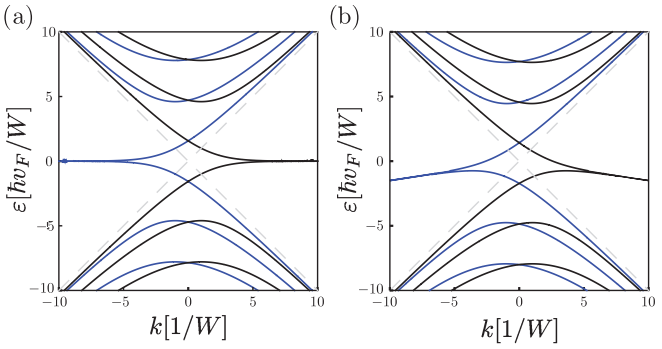

FIG. 5. (Color online) Comparison of the dispersion relations of modes in zigzag (a) and (b) reczag nanoribbons. The results for both valleys are superimposed, by measuring k relative to the K (black curves) and K'(blue curves) points, respectively. The dashed grey lines indicate the Dirac cone of graphene.

V. EFFECT OF A MAGNETIC FIELD

A. Dirac solutions

The presence of a uniform perpendicular magnetic field B_0 is accounted for by the substitution $\boldsymbol{p} \mapsto \boldsymbol{p} + e\boldsymbol{A}$, where $-e$ is the electron charge and $\boldsymbol{A} = B_0 x\hat{y}$ is the vector potential in the Landau gauge. The valleys remain uncoupled and translational invariance along the y axis is preserved. The wave function $\Psi(x,y) = \psi(x)e^{iky}$ in a single valley thus satisfies the Dirac equation

$$\psi_1 = -i\frac{\sqrt{2}}{E}\left(\partial_X + \frac{1}{2}X\right)\psi_2, \tag{5.1a}$$

$$\psi_2 = -i\frac{\sqrt{2}}{E}\left(\partial_X - \frac{1}{2}X\right)\psi_1, \tag{5.1b}$$

where $E = \varepsilon l_m/\hbar v_F$, $X = \sqrt{2}\,(x/l_m + kl_m)$, and $l_m = \sqrt{\hbar/eB_0}$ is the magnetic length.

The coupled first-order differential equations (5.1) decouple into a second-order equation,

$$\partial_X^2\psi_j(x) = \left(\tfrac{1}{4}X^2 - \tfrac{1}{2}E^2 \pm \tfrac{1}{2}\right)\psi_j(x), \tag{5.2}$$

where $j = 1,2$ and the plus sign holds for ψ_1 while the minus sign holds for ψ_2. Equation (5.2) is solved by the parabolic cylinder function $\mathcal{U}(x,a)$, determined up to normalization by[29]

$$\partial_x^2\mathcal{U} = \left(\tfrac{1}{4}x^2 + a\right)\mathcal{U}, \quad \lim_{x\to\infty}\mathcal{U}(a,x) = 0. \tag{5.3}$$

The solution in a magnetic field takes the form

$$\psi_1 = \frac{E}{\sqrt{2}}\left[A\,\mathcal{U}\left(\frac{1-E^2}{2}, X\right) - B\,\mathcal{U}\left(\frac{1-E^2}{2}, -X\right)\right], \tag{5.4a}$$

$$\psi_2 = iA\,\mathcal{U}\left(-\frac{1+E^2}{2}, X\right) + iB\,\mathcal{U}\left(-\frac{1+E^2}{2}, -X\right), \tag{5.4b}$$

where A and B are constants.

B. Edge states and Landau levels

We first consider a semi-infinite graphene sheet for $x \geqslant 0$, terminated by a B-type reczag edge at $x = 0$. Only keeping the

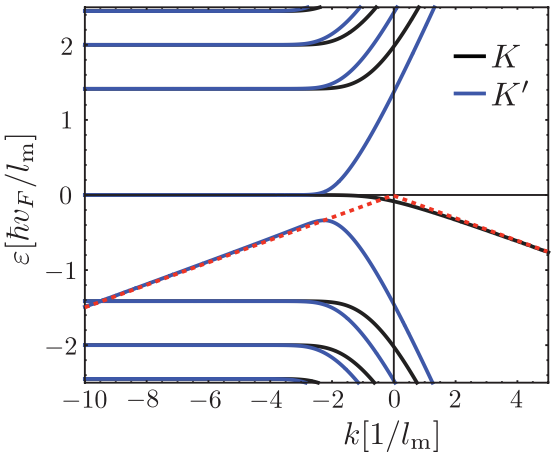

FIG. 6. (Color online) Energy dispersion at the B-type reczag edge in a magnetic field. The states in valley K and K' are shown in black and blue, respectively (with k measured relative to the respective Dirac point). The zero-field edge state dispersion is included as dashed, red lines.

solutions that decay for $x \to \infty$ in Eq. (5.4) and substituting the boundary condition (3.2), we obtain an implicit equation for the energy dispersion in the two valleys,

$$\frac{E}{\sqrt{2}} = \frac{\mathcal{U}\left(-\frac{1+E^2}{2}, \sqrt{2}kl_{\mathrm{m}}\right)}{\mathcal{U}\left(\frac{1-E^2}{2}, \sqrt{2}kl_{\mathrm{m}}\right)} \times \begin{cases} -\mathcal{F} & \text{in valley } K, \\ 1/\mathcal{F} & \text{in valley } K'. \end{cases} \tag{5.5}$$

The resulting dispersion is shown in Fig. 6. The main features can be understood from two principles: (1) the confining potential due to the magnetic field in Eq. (5.2) has its minimum at $-kl_{\mathrm{m}}^2$. Because of this, we find bulklike Landau level solutions and hence flat bands for $k \ll 0$ with the bulk Landau level energy[30] $\varepsilon_n = \mathrm{sgn}(n)(\hbar v_{\mathrm{F}}/l_{\mathrm{m}})\sqrt{2|n|}$, $n \in \mathbb{Z}$. For positive values of k, the center of the confining potential is moved beyond the edge of the sample, resulting in dispersive quantum Hall edge states with velocity v_{F} (larger than the velocity $v_{\mathrm{F}} \sin\vartheta$ of the zero-field reczag edge states). (2) The magnetic field has little effect on the reczag-edge states, if the edge-state decay length is smaller than the magnetic length, $|k \cos\vartheta|^{-1} \ll l_{\mathrm{m}}$. For this reason, we observe two bands in Fig. 6 that follow the reczag edge dispersion (shown as dashed lines) for large enough momenta.

C. Triple edge mode in the lowest Landau level

The interplay of the magnetic and zero-field edge states produces three distinct edge modes in the lowest Landau level ($n = 0$). These are labeled a, b, and c in the top panel of Fig. 7. The unidirectional edge mode a in valley K is accompanied by a pair of counterpropagating edge modes in valley K'. These three modes have a distinct wave function profile, as shown in the lower panels of Fig. 7.

For mode a in the K valley, the bulk Landau level solution for $k \ll 0$ is nonzero on the B sublattice only.[30] It moves closer to the edge with increasing k and eventually becomes the reczag edge state, which is mostly localized on sublattice B with a small $\mathcal{O}(\mathcal{F}^2)$ contribution on the A sublattice. In contrast, for modes $b$and$c$ in the K' valley, there are two solutions for every momentum; for $k \ll 0$, we find both the

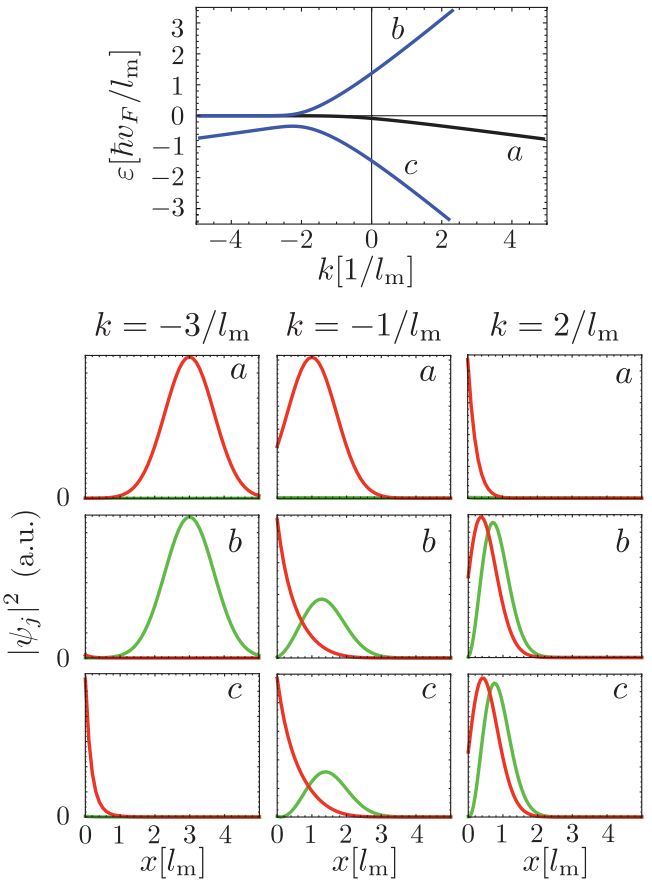

FIG. 7. (Color online) Nine lower panels: probability density profiles for three different values of k in the three distinct modes of the lowest Landau level, labeled a, b, and c in the top panel. Mode a is in valley K and the counter-propagating modes b and c are in valley K'. The colors distinguish the probability densities on sublattice A (green) and B (red). To allow a comparison of the profiles, the vertical axis in each graph has been rescaled.

bulk Landau level solution (localized on sublattice A only) and the reczag edge state (localized mostly on sublattice B). Note that we find bands with a distinct bulk or edge character, in contrast to the zigzag edge where chiral symmetry forces always hybridized solutions.[31]

The tripling of the edge modes in the lowest Landau level does not change the value of the Hall conductance, since the contribution from the two counterpropagating modes cancels. But the valley polarization at the edge is changed. At a zigzag edge, the lowest Landau level edge modes are in the same valley for positive and negative energies, whereas they are in different valleys at an armchair edge.[32] At the reczag edge both valleys are present for negative energy with only a single valley for positive energy.

D. Comparison with tight-binding model

Figure 8 shows a comparison between the band structure obtained from the Dirac equation and from the tight-binding model. (Similar tight-binding calculations are in Refs. 19 and 21.) To be able to identify the contributions from the two edges, we took a wide nanoribbon, $W = 8\,l_{\mathrm{m}} = 101\sqrt{3}/2a$, in which opposite edges are approximately decoupled. In this

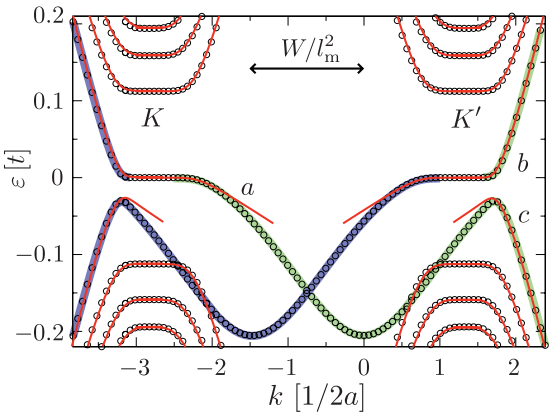

FIG. 8. (Color online) Comparison of the energy dispersion of a reczag nanoribbon in a magnetic field obtained from the tight-binding model (open circles) and from the Dirac equation (red lines). For the lowest Landau level, the edge states localized at the $x = 0$ and $x = W$ boundary are highlighted in green and blue, respectively. The three lowest-Landau-level modes at the $x = 0$ edge are labeled a, b, and c. They appear displaced relative to Fig. 7, because there the momentum k is measured relative to the Dirac point of valley K and K'.

case, the Dirac equation results for the A-type reczag edge at $x = W$ can be directly obtained from the results for a B-type reczag edge at $x = 0$ by interchanging the valleys and replacing $k \to -k - W/l_m^2$.

The two calculations agree very well near the Dirac points. As in the zero-field case [see Fig. 3(b)], the tight-binding model connects the edge states from the two valleys K and K', which are disconnected in the Dirac equation.

VI. CONCLUSION

In conclusion, we have derived the boundary condition for the Dirac equation at reconstructed zigzag edges in graphene. The ϑ class of boundary conditions (2.8) applies to reconstructions with a unit cell that is not a multiple of three times the zigzag unit cell. We have calculated the angular parameter ϑ for the zz(57) (reczag) reconstruction, which has been identified as the most stable reconstruction. Most of our results are given for general $|\vartheta| < \pi/2$, so they apply to other reconstructions in the ϑ class as well.

The ϑ-class reconstructions share two key properties: they do not cause intervalley scattering and they support edge states. Dispersive edge states were previously found for the reczag edge,[21] the zigzag edge with next-nearest neighbor hopping,[33] and the zigzag edge with a boundary potential.[34] Our analysis identifies an entire class of reconstructions with edge states and gives analytic expressions for the edge state dispersion in terms of a single parameter ϑ.

The edge mode appears in the local density of states as a peak at energy $\varepsilon_{\rm peak}$. The dependence of $\varepsilon_{\rm peak}$ on the separation x from the edge, given by Eq. (4.15), allows a direct measurement of ϑ by scanning tunneling microscopy.

In a magnetic field, there appears a tripling of the edge modes in the lowest Landau level. This could be observed in transport experiments, since two of three edge modes are counterpropagating and therefore susceptible to localization by disorder. With increasing disorder, the two-terminal conductance would then be reduced by a factor 1/3.

ACKNOWLEDGMENTS

We thank A. Fasolino for drawing our attention to this problem. Our research was supported by the Dutch Science Foundation NWO/FOM, the Eurocores program EuroGraphene, and an ERC Advanced Investigator grant.

APPENDIX A: CONDITION FOR ABSENCE OF VALLEY MIXING BY EDGE RECONSTRUCTION

We explain the zone-folding argument used in Sec. III A to identify which periodicity of the edge reconstruction leaves the valleys uncoupled. It is similar to the zone-folding argument that distinguishes metallic and semiconducting carbon nanotubes.[35]

The projection of the K point along the direction of the edge is given by

$$\boldsymbol{K} \cdot \frac{\boldsymbol{T}}{|\boldsymbol{T}|} = \frac{1}{3}(n-m)\frac{2\pi}{|\boldsymbol{T}|}, \tag{A1}$$

and the projection of the K' point by

$$\boldsymbol{K'} \cdot \frac{\boldsymbol{T}}{|\boldsymbol{T}|} = \frac{1}{3}(m-n)\frac{2\pi}{|\boldsymbol{T}|}. \tag{A2}$$

The projected K and K' points correspond to the same momentum in the one-dimensional first Brillouin zone of the edge, if they differ by a multiple of a reciprocal lattice vector. This condition $(\boldsymbol{K} - \boldsymbol{K'}) \cdot \boldsymbol{T}/|\boldsymbol{T}| = l\,2\pi/|\boldsymbol{T}|$, $l \in \mathbb{Z}$, is equivalent to the condition that $n - m$ is divisible by three. Otherwise, if $n \neq m$ mod 3, the K points project to different momenta in the first Brillouin zone of the edge, and since these momenta are conserved due to translational symmetry, the valleys remain uncoupled.

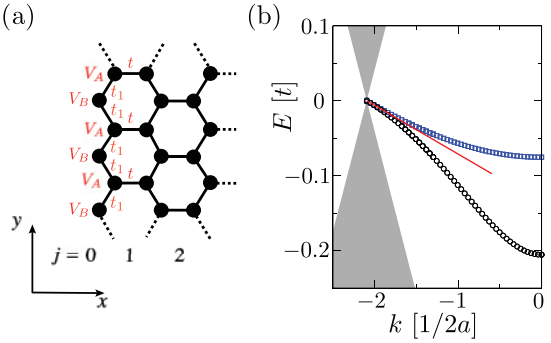

FIG. 9. (Color online) (a) Schematic of the modified zigzag edge with on-site potentials and hoppings labeled in red. (b) Comparison between the tight-binding edge state dispersion for the reczag (black circles) and the modified zigzag edges with $V_A = 0$, $t_1 = t$, $V_B = -\mathcal{F}t$ (blue squares). The Dirac equation has the same boundary condition at these two edges, leading to the same edge state dispersion near the Dirac point (red solid line).

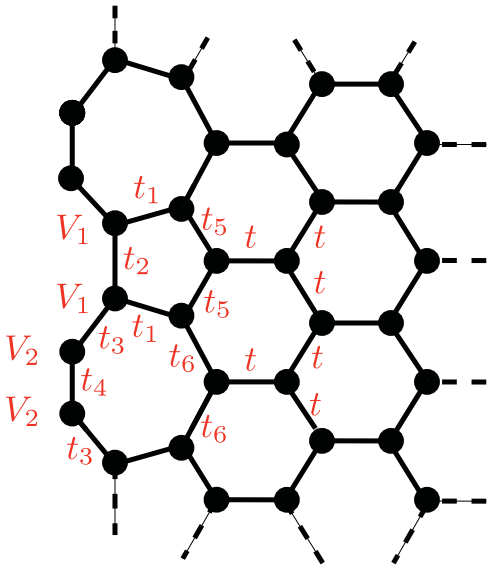

FIG. 10. (Color online) Schematic of the extended model for the reczag edge with on-site energies and hoppings labeled in red.

APPENDIX B: BOUNDARY CONDITION FOR MODIFIED ZIGZAG EDGE

Edge reconstruction is one modification of the zigzag edge that leads to a boundary condition of the single-parameter form (2.8). In this appendix, we calculate the value of the parameter ϑ for two alternative modifications of the zigzag edge that break chiral symmetry: on-site potentials and next-nearest-neighbor hopping. Since most of our results for the reczag edge are given for arbitrary ϑ, they can be applied to these edges as well—even though these modifications leave the lattice structure unaffected.

Consider a B-type zigzag edge with a nonzero potential V_A, V_B on the outermost A and B atoms, see Fig. 9(a). Such on-site potentials could appear because the edge atoms see a different chemical environment than the bulk atoms. We also include a possible modification t_1 of the hopping amplitude at the edge. The same model with $V_B = -t'$ describes to leading order the effect of a next-nearest-neighbor hopping t'.[36]

Since the unit cell is not changed by these modifications, the boundary modes that appeared for the reczag edge are absent. Following the approach of Sec. III, we find

$$\mathcal{F} = \tan(\vartheta/2) = \frac{t V_B}{V_A V_B - t_1^2}\,. \tag{B1}$$

This agrees with Refs. 28 and 34 for the special case $V_A = 0$, $t_1 = t$. If next-nearest-neighbor hopping is the only modification, we set $V_B = -t'$, $V_A = 0$, $t_1 = t$ and arrive at

$$\mathcal{F} = \tan(\vartheta/2) = t'/t\,. \tag{B2}$$

Figure 9(b) shows a comparison of the edge state dispersion for the reczag edge from Sec. III and a zigzag edge with an edge potential such that the value of $\mathcal{F}$ is the same. Both have the same boundary condition for the Dirac equation, and indeed, we observe the same linearly dispersing edge state close to the Dirac point.

TABLE II. Values of the hopping amplitudes in the extended tight-binding model, obtained from DFT.[21] In this model, $V_1 = V_2 = 0$. The boundary condition parameter is calculated from Eq. (C1).

t_1/t	t_2/t	t_3/t	t_4/t	t_5/t	t_6/t	$\mathcal{F}$	ϑ
0.94	0.94	1.06	1.42	1.04	0.98	0.0485	0.0968

APPENDIX C: EXTENDED MODEL FOR THE RECZAG EDGE

The tight-binding model for the reczag edge used in the main text is based on Ref. 19. An extended model was studied in Ref. 21, including also modifications of the hopping amplitudes in the first row of hexagons near the edge. From the general arguments of Sec. II, we know that the form of the boundary condition remains the same, with a different numerical value for the parameter ϑ. In this appendix, we calculate that value.

The extended model of the reczag edge is shown in Fig. 10. In addition to the modified hopping amplitudes of Ref. 21, we also include (for additional generality) an on-site potential at the outermost edge atoms. Following the same procedure as in Sec. III, we obtain

$$\mathcal{F} = \tan(\vartheta/2) = \mathcal{T}/\mathcal{N}, \tag{C1}$$

as the ratio of the coefficients

$$\begin{aligned}\mathcal{T} = t t_1^2\{&[t_2(2t_5^2 + 2t_5t_6 - t_6^2) - 2(t_5^2 + t_5t_6 + t_6^2)V_1] \\ &\times (t_4^2 - V_2^2) + t_3^2[t_4(t_5^2 - 2t_5t_6 - 2t_6^2) \\ &- 2(t_5^2 + t_5t_6 + t_6^2)V_2]\},\end{aligned} \tag{C2}$$

$$\mathcal{N} = 6t_5^2t_6^2[t_3^4 + (t_2^2 - V_1^2)(t_4^2 - V_2^2) + t_3^2(t_2t_4 - 2V_1V_2)]. \tag{C3}$$

Using the numerical values from Ref. 21, see Table II, we find $\vartheta \approx 0.0968$, which is within a factor of two from the value $\vartheta \approx 0.150$ following from the simpler model of Table I.

[1] A. H. Castro Neto, F. Guinea, N. M. R. Peres, K. S. Novoselov, and A. K. Geim, Rev. Mod. Phys. **81**, 109 (2009).
[2] L. Brey and H. A. Fertig, Phys. Rev. B **73**, 235411 (2006).
[3] M. Fujita, K. Wakabayashi, K. Nakada, and K. Kusakabe, J. Phys. Soc. Jpn. **65**, 1920 (1996).
[4] K. Nakada, M. Fujita, G. Dresselhaus, and M. S. Dresselhaus, Phys. Rev. B **54**, 17954 (1996).
[5] Y.-W. Son, M. L. Cohen, and S. G. Louie, Nature (London) **444**, 347 (2006).
[6] K. A. Ritter and J. W. Lyding, Nat. Mater. **8**, 235 (2009).
[7] Y. Niimi, T. Matsui, H. Kambara, K. Tagami, M. Tsukada, and H. Fukuyama, Phys. Rev. B **73**, 085421 (2006).
[8] Y. Kobayashi, K. I. Fukui, T. Enoki, and K. Kusakabe, Phys. Rev. B **73**, 125415 (2006).

[9]C. Tao, L. Jiao, O. V. Yazyev, Y.-C. Chen, J. Feng, X. Zhang, R. B. Capaz, J. M. Tour, A. Zettl, S. G. Louie, H. Dai, and M. F. Crommie, Nat. Phys. **7**, 616 (2011).

[10]P. Koskinen, S. Malola, and H. Häkkinen, Phys. Rev. Lett. **101**, 115502 (2008).

[11]T. Wassmann, A. P. Seitsonen, A. M. Saitta, M. Lazzeri, and F. Mauri, Phys. Rev. Lett. **101**, 096402 (2008).

[12]B. Huang, M. Liu, N. Su, J. Wu, W. Duan, B.-L. Gu, and F. Liu, Phys. Rev. Lett. **102**, 166404 (2009).

[13]J. Li, Z. Li, G. Zhou, Z. Liu, J. Wu, B.-L. Gu, J. Ihm, and W. Duan, Phys. Rev. B **82**, 115410 (2010).

[14]G.-D. Lee, C. Z. Wang, E. Yoon, N.-M. Hwang, and K. M. Ho, Phys. Rev. B **81**, 195419 (2010).

[15]C. K. Gan and D. J. Srolovitz, Phys. Rev. B **81**, 125445 (2010).

[16]J. M. H. Kroes, M. A. Akhukov, J. H. Los, N. Pineau, and A. Fasolino, Phys. Rev. B **83**, 165411 (2011).

[17]P. Koskinen, S. Malola, and H. Häkkinen, Phys. Rev. B **80**, 073401 (2009).

[18]C. Girit, J. C. Meyer, R. Erni, M. D. Rossell, C. Kisielowski, L. Yang, C.-H. Park, M. F. Crommie, M. L. Cohen, S. G. Louie, and A. Zettl, Science **323**, 1705 (2009).

[19]P. Rakyta, A. Kormányos, J. Cserti, and P. Koskinen, Phys. Rev. B **81**, 115411 (2010).

[20]S. M.-M. Dubois, A. Lopez-Bezanilla, A. Cresti, F. Triozon, B. Biel, J.-C. Charlier, and S. Roche, ACS Nano **4**, 1971 (2010).

[21]J. N. B. Rodrigues, P. A. D. Gonçalves, N. F. G. Rodrigues, R. M. Ribeiro, J. M. B. Lopes dos Santos, and N. M. R. Peres, Phys. Rev. B **84**, 155435 (2011).

[22]J. W. McClure, Phys. Rev. **104**, 666 (1956).

[23]D. P. DiVincenzo and E. J. Mele, Phys. Rev. B **29**, 1685 (1984).

[24]A. R. Akhmerov and C. W. J. Beenakker, Phys. Rev. B **77**, 085423 (2008).

[25]V. A. Volkov and I. V. Zagorodnev, Low Temp. Phys. **35**, 2 (2009).

[26]Reference 21 reaches a different conclusion that the decay lengths into the bulk differ for the two sublattices in the case of a reczag edge. In their tight-binding approach, the Dirac and boundary modes are not easily separated. While we find that the former have a sublattice independent decay length $\simeq 1/k$, the latter modes do introduce a sublattice dependence on the scale of the lattice constant, in accordance with Eq. (3.11).

[27]M. Wimmer, A. R. Akhmerov, and F. Guinea, Phys. Rev. B **82**, 045409 (2010).

[28]J. Wurm, K. Richter, and I. Adagideli, Phys. Rev. B **84**, 075468 (2011).

[29]M. Abramowitz and I. A. Stegun, *Handbook of Mathematical Functions* (Dover, New York, 1972).

[30]T. Ando, J. Phys. Soc. Jpn. **74**, 777 (2005).

[31]L. Brey and H. A. Fertig, Phys. Rev. B **73**, 195408 (2006).

[32]A. R. Akhmerov and C. W. J. Beenakker, Phys. Rev. Lett. **98**, 157003 (2007).

[33]K. Sasaki, S. Murakami, and R. Saito, Appl. Phys. Lett. **88**, 113110 (2006).

[34]S. Bhowmick and V. B. Shenoy, Phys. Rev. B **82**, 155448 (2010).

[35]R. Saito, G. Dresselhaus, and M. S. Dresselhaus, *Physical Properties of Carbon Nanotubes* (Imperial College, London, 2003).

[36]K. I. Sasaki, Y. Shimomura, Y. Takane, and K. Wakabayashi, Phys. Rev. Lett. **102**, 146806 (2009).